Supplementary Material for

Polarization saturation in multi-layered interfacial ferroelectrics

Wei Cao[1#], Swarup Deb[2#], Maayan Vizner Stern[2#], Noam Raab[2], Michael Urbakh[1], Oded Hod[1], Leeor Kronik[3], Moshe Ben Shalom[2]

1 Department of Physical Chemistry, School of Chemistry, The Raymond and Beverly Sackler Faculty of Exact Sciences and The Sackler Center for Computational Molecular and Materials Science, Tel Aviv University, Tel Aviv 6997801, Israel.

2 School of Physics and Astronomy, Tel Aviv University, Tel Aviv 6997801, Israel

3 Department of Molecular Chemistry and Materials Science,
Weizmann Institute of Science, Rehovoth 7610001, Israel

# These authors contributed equally

Table of Contents

S1. Materials and measurements

S1.1. Device Fabrication

MoS_2 flakes of various thicknesses were exfoliated from a bulk 3R crystal, obtained from ″HQ Graphene″, onto SiO_2/Si substrates. Few-nm thick flakes with topographic steps of single layers were selected. An atomic force microscope (AFM) was used to scan the flake's topography.

S1.2. AFM Measurements

Topography and Kelvin probe force microscopy (KPFM) measurements were performed using a Park System NX10 AFM, employing PPP-EFM n-doped tips with conductive coating. The mechanical resonance frequency of the tip was 75 kHz, its force constant was 3 N/m, and the cantilever was oscillated mechanically with an amplitude of ~20 nm. Amplitude-modulated KPFM (AM-KPFM) measurements are known to produce poor spatial resolution and severely underestimate the measured surface potential, particularly for microscopic samples. Non-local electrostatic interaction of the sample with the cone and cantilever of the scanning tip has been identified as the primary reason behind it. To overcome this issue and to gain a more localized response, we have used frequency-modulated KPFM (FM-KPFM) or sideband KPFM, which is sensitive to electrostatic interaction variation rather than the interaction strength itself.(*1*) Therefore, the sideband signal has the highest contribution from the tip apex, which has the smallest dimension and is the closest to the surface. We note that this type of global external measurement still slightly averages the desired signal with additional signal from the surroundings and thus provides a lower limit to the measured ΔV value. In our measurements, we excite the cantilever with an AC voltage amplitude of 2V and a frequency of 2 kHz. The topography and the KPFM signals were obtained separately using a two-pass measurement. The first pass recorded the topography in non-contact mode. In the second pass, the KPFM potential was recorded after lifting the tip an extra 5 nm and following the same topography line-scan, ensuring separation of the topography and the electrical signals. The images in Fig. 1 and S1 were acquired using Park SmartScan software and the data analysis was performed with the Gwyddion program.

S1.3. Additional Examples

Device 2

Fig. S1 presents an additional demonstration of the polarization saturation for another device (device 2). The noise is analyzed as the standard deviation of the potential at a clean region of a few μm^2 and is typically less than 20mV (see the error bars in Fig. 1d and Fig. S1). We note that surface contaminants and the noise level tend to accumulate at high potentials and are challenging to avoid, although the inert atmosphere in our microscope.

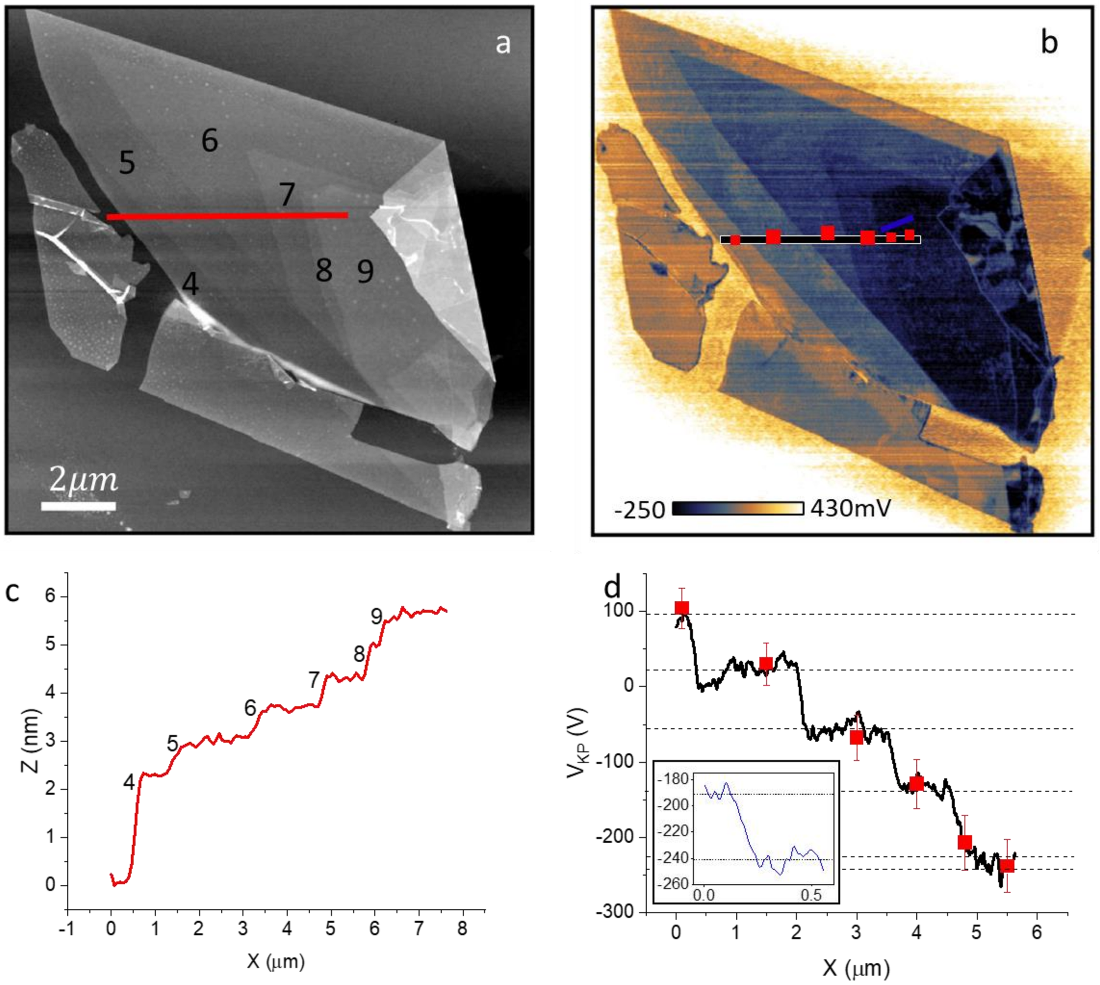

Figure S1. Additional example of polarization saturation. Topography (a) and Surface potential (b) maps, measured using AFM and KPFM, respectively. (c) A cross section taken along the red line in (a). (d) A cross section taken along the red (inset: blue) line in b.

Devices 3+4

The flakes corresponding to devices 3 and 4 were transferred onto a graphite substrate and cleaned *in situ* before the KPFM measurements in our vacuum AFM. Fig. S2 presents additional demonstrations of the polarization saturation for devices with non-uniform domains. We observed similar trends in the voltage dependence on the number of layers. We have included the data from these additional devices in Fig. S2 of the supplementary information and incorporated it into Fig. 2a of the main text.

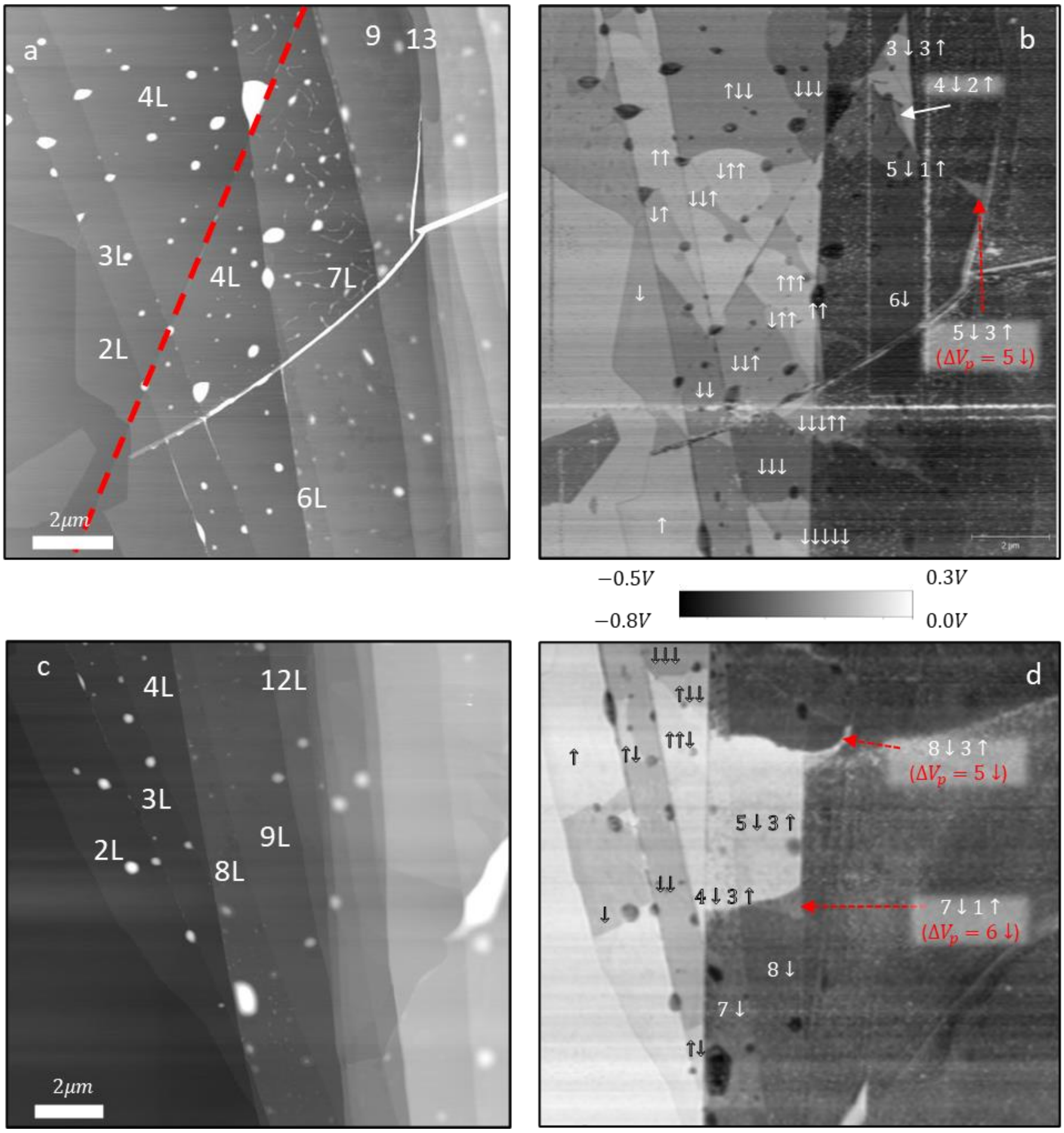

Figure S2. Additional examples of polarization saturation in multi-domain flakes. Topography (a,c) and Surface potential (b,d) maps, obtained from AFM and KPFM measurements, respectively, for devices 3 and 4. Here the flakes are placed on a ~ 10 nm graphite flake. The number of layers is annotated on the topography images. In the surface potential maps, arrows indicate the number of polarized interfaces pointing up and down (↑ , ↓). Note that even for $N > N_{saturation} \approx 8$, as long as $|N_{\uparrow} - N_{\downarrow}| < N_{saturation}$, the surface potential accumulates in a linear fashion (see red arrows in b,d).

S1.4. Comparison of the calculated electric potential with KPFM measurements

To facilitate comparison between the data and the calculated electric potential, the data in Fig. 2a are plotted with shifted absolute values. The calculated electric potential for a stack of N MoS_2 layers, $V(N)$, is referenced to $V(1)$. In practice, we shifted all the data relative to the minimum layer measurement, corresponding to *N=2* for devices 1, 3, 4 and *N=4* for device 2, with 1 and 3 interfaces, respectively. We then added a correction, ΔV, for changing the reference to $V(1)$. In other words, the plotted data show $|V(N) - V(2)| + \Delta V$ for devices 1, 3, 4 and $|V(N) - V(4)| + 3\Delta V$ for device 2 (where ΔV is the average measured potential step in the linear regime, the values of which for the four devices are 56, 78, 63, and 73 meV, as also mentioned in the main text).

S2. Additional details regarding the DFT calculations

S2.1. Computational details

DFT methods

To obtain the electrostatic potential of the multilayer *r*-MoS_2 stack shown in Fig. 2, we used the Perdew-Burke-Ernzerhof (PBE) generalized-gradient exchange-correlation density functional approximation,(*2*) augmented by the Grimme-D3 dispersion correction using Becke-Johnson (BJ) damping,(*3*) as implemented in the Vienna Ab-initio Simulation Package (VASP)(*4*). A plane wave energy cutoff of 600 eV and a k-point mesh of 20×20×1 were used, with a vertical vacuum size of 10 nm to avoid interactions between adjacent images. The core electrons of the atoms were treated via the projector augmented wave (PAW) approach. The 3R stacked structures were constructed and relaxed using the conjugated gradients algorithm with a force threshold of 10^{-3} eV/Å. Single-point electron density calculations were then performed on the relaxed structure using a Gaussian smearing of 0.05 eV, to enhance the convergence of the self-consistent cycle. The same approach was used to calculate the potential differences of WSe_2 and *r*-BN that are shown in Fig. 2b.

Consistency and convergence tests

To evaluate the vertical polarization, a dipole moment correction was employed.(*5*) For validation purposes, doubled supercell calculations were also performed, yielding nearly identical potential differences (see Fig. S3a). The doubled supercell consists of two opposing mirror images of each MoS_2 stack with a 6 nm inter-image vacuum region. Fig. S3b and S3c show the potential profiles along the normal direction calculated by the dipole correction and double supercell methods for N=14, respectively.

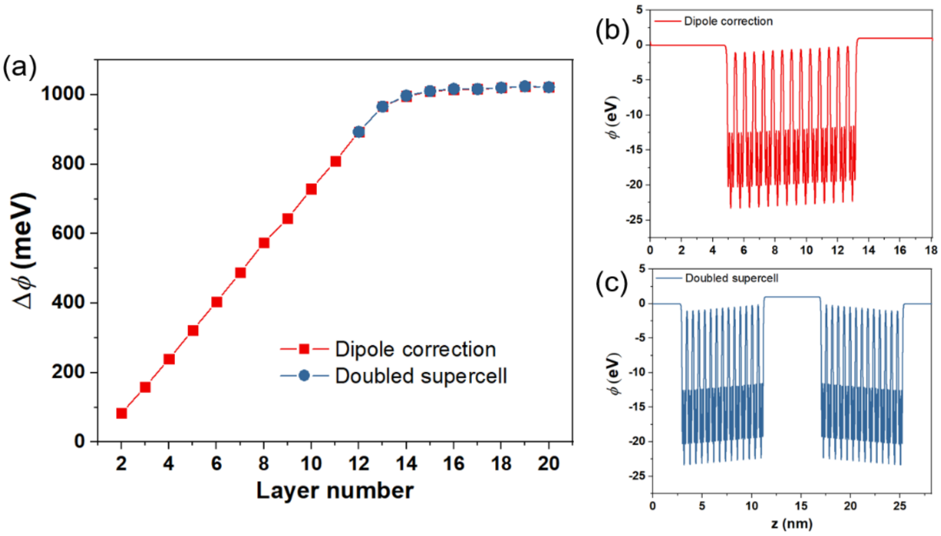

Figure S3. Potential difference calculations. (a) Potential drop as a function of number of layers calculated by the dipole correction and a doubled supercell setup for multilayer *r*-MoS_2. Potential profiles of the N=14 layer system calculated by the (b) dipole correction method and (c) doubled supercell approach.

Convergence tests of the calculations (Fig. S4) indicate that our choice of parameters leads to electrostatic potential differences convergence to within 2.5, 0.1, and 0.7 meV with respect to the number of k-points, energy cut-off, and vacuum size, respectively. The corresponding total energy convergence values are to within 0.04, 8, and 0.7 meV.

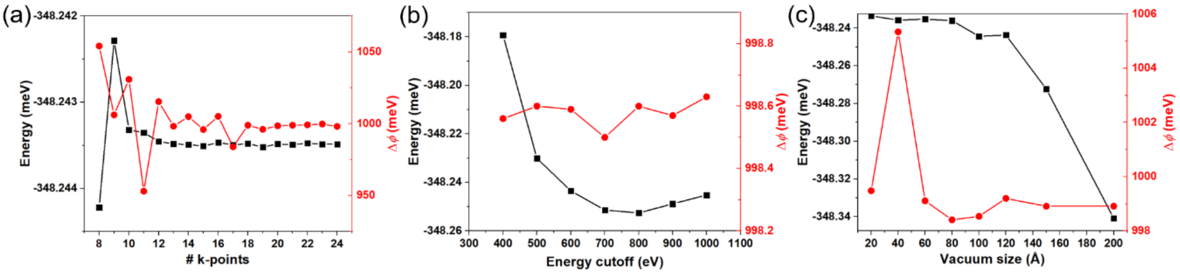

Figure S4. Convergence tests. Convergence tests of the total energy (black curve, left vertical axis) and electrostatic potential difference (red curve, right vertical axis) of N=16 MoS_2 as a function of: (a) number of k-points, (b) energy cutoff, and (c) vacuum size.

Effect of geometry relaxation

Fig. S5 shows a comparison of the potential drop and bandgap calculations for unrelaxed and relaxed multilayer *r*-MoS_2. In the former, only the geometry of individual layers is relaxed, as described above, whereas in the latter an additional geometry relaxation step is undertaken for the entire stack. Both the saturation curve and the bandgap dependence on number of layers are weakly affected by stack geometry relaxation, indicating that the polarization saturation mechanism is dominated by electronic, rather than structural, effects.

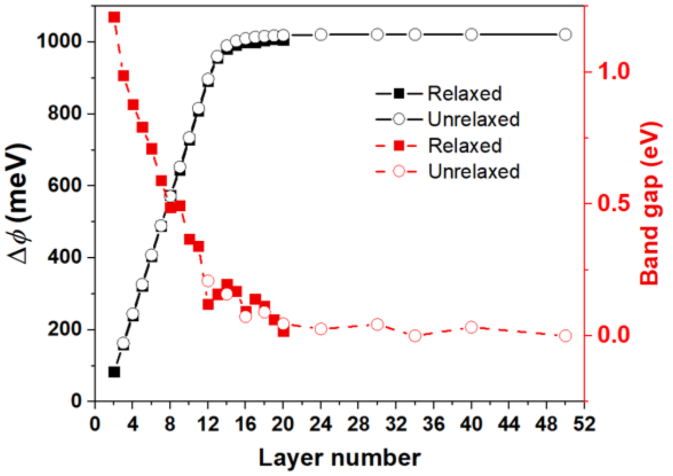

Figure S5. Effect of geometry relaxation. The potential difference (black, left) and band gap (red, right) of *r*-MoS_2 as a function of layer number before (open symbols) and after (full symbols) stack geometry relaxation.

Hybrid functional and spin-orbit coupling calculations

The polarization saturation shown in the main text was performed at the PBE level of theory, excluding spin-orbit coupling (SOC) effects. To evaluate both the effect of the exchange-correlation density functional approximation and the possible role of SOC contributions, we performed additional single-point polarization calculation using the PBE optimized multilayer *r*-MoS_2 model systems, either at the Heyd-Scuseria-Ernzerhof (HSE)(*6-9*) screened-exchange hybrid density functional level of theory, or with scalar-relativistic corrections. Fig. S6 demonstrates that while the HSE bandgap is consistently larger than the PBE one and SOC induces band splitting, at the linear commulative region replacement of PBE by HSE or the inclusion of SOC has an insignificant effect on the calculated polarization.

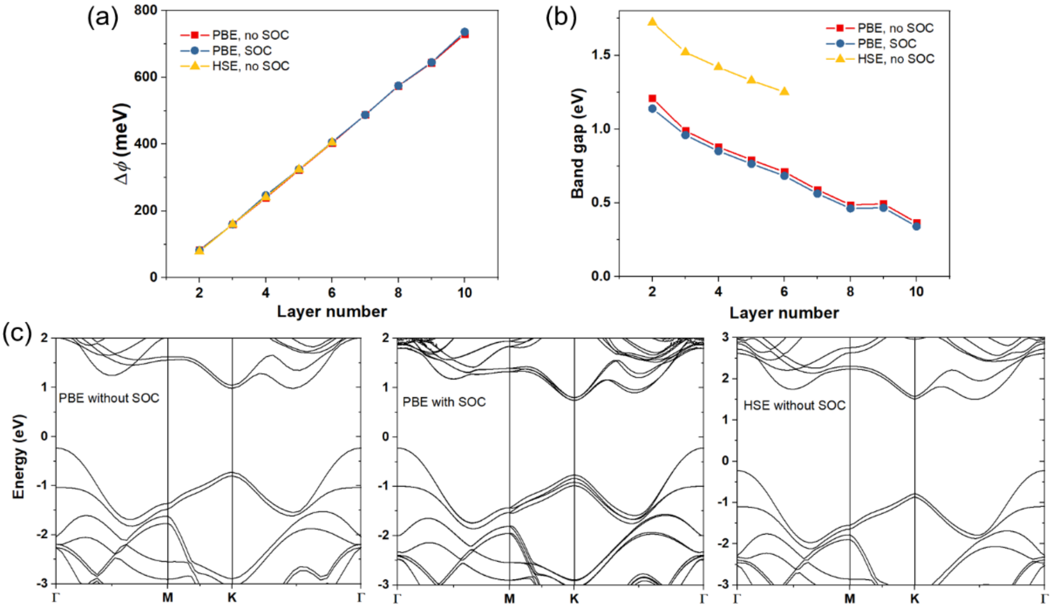

Figure S6. Screened-hybrid functional and spin-orbit coupling calculations. (a) Potential drop and (b) bandgap as a function of number of layers obtained using the PBE functional approximation, without (red) and with SOC (blue), and with the HSE functional without SOC (yellow). (c) Corresponding band structures of four-layered *r*-MoS_2.

Doping calculations

To perform DFT calculations that include effective doping, multilayer *r*-MoS_2 stacks were first geometrically relaxed as described above. This was followed by single-point calculations using the fractional nuclear charge pseudoatom approach,(*10*) as implemented in the Quantum Espresso open source package(*11*). A doping density of 7.5×10^{11} cm^{-2} per layer was imposed through fractional charging of both the Mo and S nuclei with an extra charge of 2.16×10^{-4} |e|. An energy cutoff of 60 Ry (816.34 eV) was used with a larger k-point grid of 30 × 30 × 1 (found necessary for convergence) and a vertical vacuum size of 10 nm to avoid spurious interactions between adjacent bilayer images. Fermi-Dirac smearing with an effective temperature of ~300 K was used to enhance the convergence of the self-consistent cycle.

To confirm that the calculations employing effective doping do not affect the band structure, we conducted a comparative analysis of the band structure and density of states (DOS) between the undoped and doped 12-layer *r*-MoS_2 stack, shown in Fig. S7a. They are additionally compared to the same analysis for non-polar 2H stacked MoS_2, as shown in Fig. S7b. In the latter case, minimal band changes are observed, other than a trivial uniform shift, thereby validating the effective doping approach. For the polar layers, doping results in an increase in the band gap, but the DOS curves clearly establish that this is attributed to polarization-induced band shifts, rather than deformation of the bands themselves.

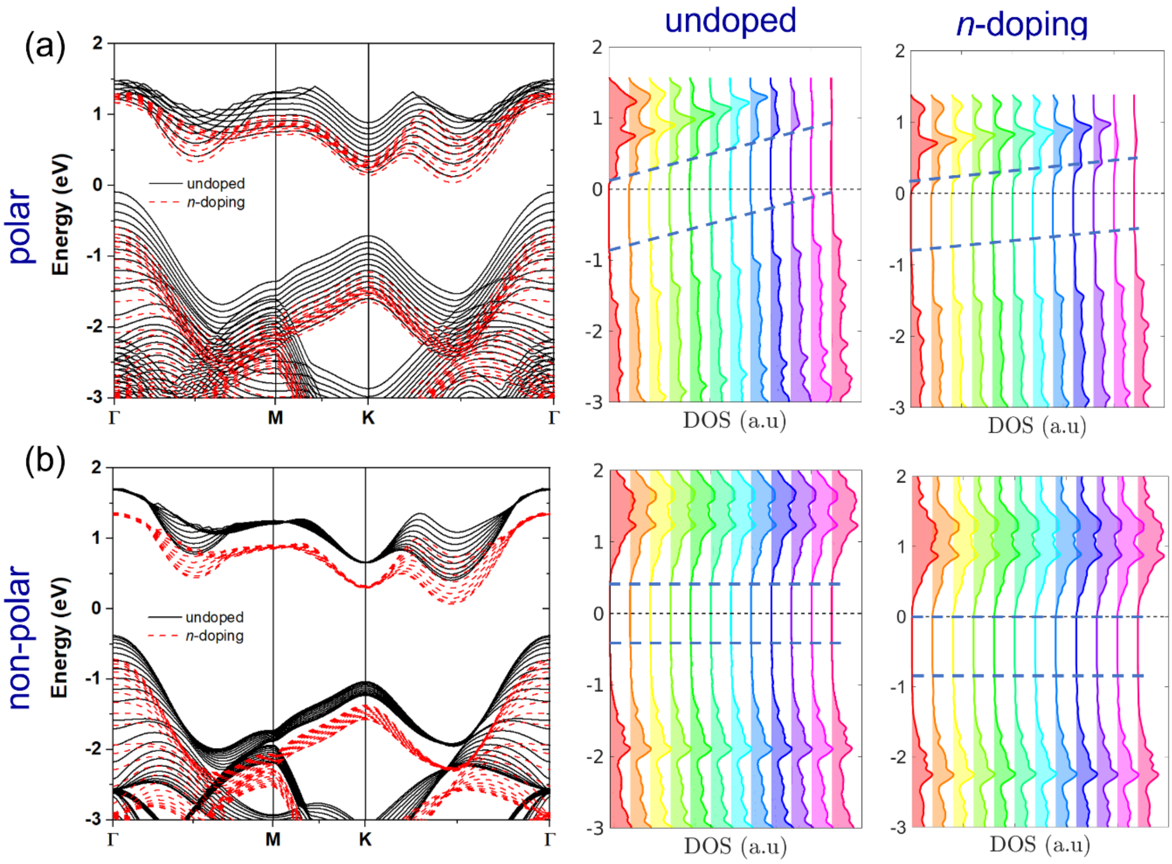

Figure S7. Demonstration of the validity of doping calculations. The band structures and density of states (DOS) obtained via DFT calculations for an undoped and doped (charge carrier density of $7.5 \cdot 10^{11}$ $e \cdot cm^{-2}$ per layer) 12-layer (a) rhombohedral (polar) and (b) AA' (non-polar) MoS_2 stack. The energy origin is set to the Fermi level. The blue dashed lines denote the changing position of the local valence band maximum (VBM) and the conduction band minimum (CBM) across the stack.

S2.2. DFT calculated MoS_2 density of states

In Fig. 3a of the main text, we show the DFT calculated density of states projected onto the various layer of a 15-layered *r*-MoS_2 stack. For completeness, we present in Fig. S8 similar results for systems of different thickness ($N = 9$, 12, and 18). The slopes of the VBM and CBM spatial variations for the $N = 9$ and 12 systems are similar, whereas for the $N = 18$ system, which is already above the polarization saturation thickness, a lower slope is obtained.

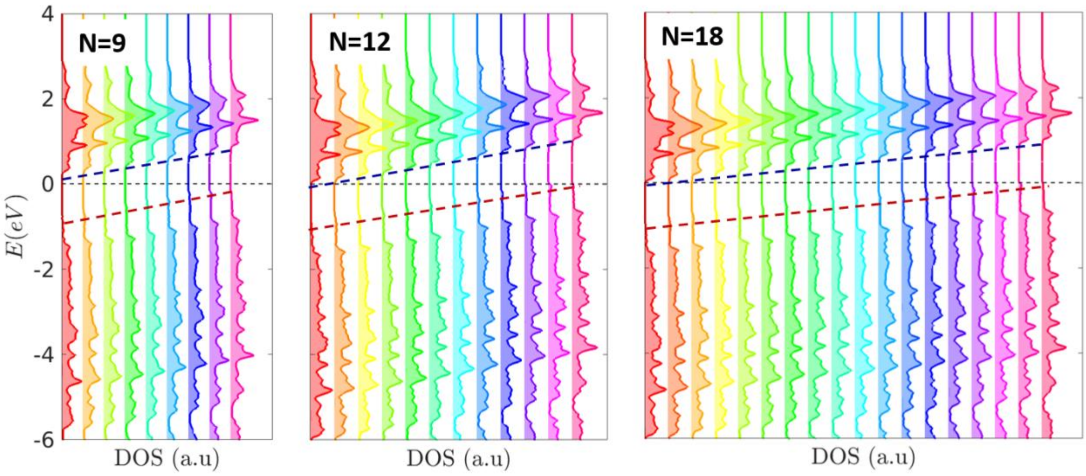

Figure S8. DFT calculated DOS. DFT calculated density of states projected onto the various layer of a r-MoS_2 stack consisting of $N = 9$, 12, or 18 layers.

S2.3. Potential profile of MoS_2

The charge transfer between the stacked layers is understood by the potential distribution, as illustrated in Fig. S9. The laterally-averaged electrostatic potential profiles, relative to individual monolayers, for N=12 (Fig. S9a) and N=16 (Fig. S9b) are depicted. Both systems demonstrate uniformly spaced and decoupled potential steps. In the case of the 12-layer configuration, the potential step size matches the potential drop observed in bilayer AB stacked MoS_2 (i.e., 83 meV). In contrast, the potential step size in the 16-layer system is smaller, as saturation has already set in.

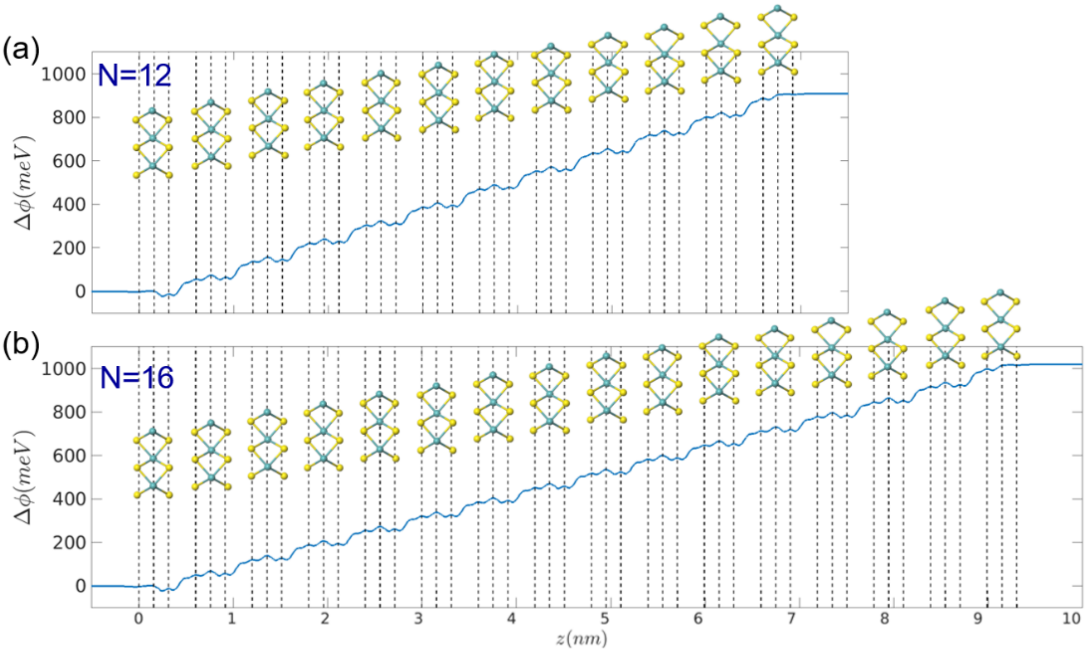

Figure S9. Potential distributions analysis. Difference between the laterally-averaged potential profile obtained for *r*-MoS_2 with (a) $N = 12$ and (b) N=16 layers and that of the corresponding monolayers. The black dashed lines represent the vertical locations of the ions. The origin of the horizontal axis is set to the bottom S sublayer.

S2.4. Estimation of polarization saturation

Table S1 shows the prediction of polarization saturation for *r*-MoS_2, *r*-WSe_2, and *r*-BN stacks, yielding the critical thickness, N_c, compared to the one predicted from the bandgap.

Table S1. Prediction of polarization saturation thickness by the potential drop associated with a single interface, V_I, and the bandgap, E_g, of a bulk *r*-MoS_2, *r*-WSe_2, and *r*-BN, under periodic boundary conditions.

Type	$V_I\ (meV)$	$E_g(eV)$	N_c	
			Prediction	Calculation
MoS_2	82	0.896	12	14
WSe_2	69	0.992	16	18
h-BN	115	4.136	37	40

S2.5. Band gap of MoS_2, *r*-WSe_2 and *r*-BN as a function of stack thickness

In Fig. 2b in the main text we compare the saturation characteristics of *r*-MoS_2, *r*-WSe_2 and *r*-BN. In Fig. S10a, we present the stack thickness dependence of the bandgap of bernal (labled as AB(A), blue), rhombohedral (labeled as AB(C), yellow), and AA’ (red) stacked

MoS_2. By comparing the polar stacking behavior (yellow) to the non-polar configurations (blue and red), we observe that the latter converge to a finite value, whereas the former approaches bandgap closure following the mechanism discussed in the main text. Similar bandgap closure is seen also for *r*-WSe_2 (Fig. S10b) and *r*-BN (Fig. S10c) polar multilayers.

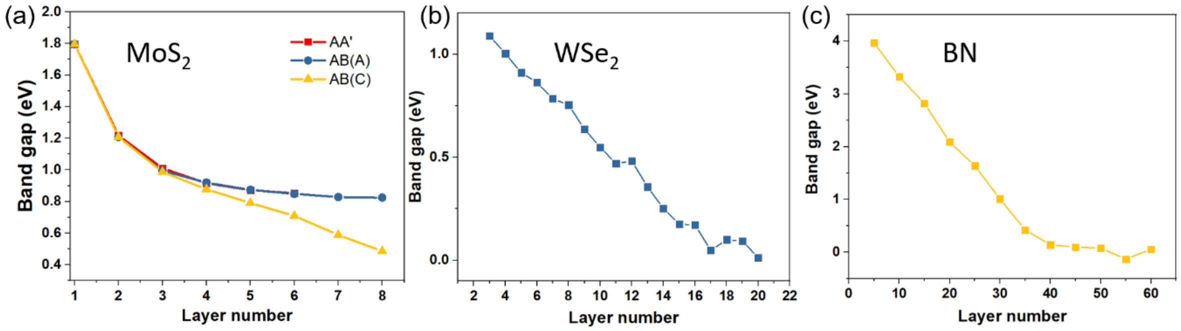

Figure S10. Band gap of *r*-MoS_2, *r*-WSe_2, and *r*-BN. (a) Bandgap of multilayer r-MoS_2 at various stacking modes, as a function of number of layers. (b), (c) Bandgap of multilayer *r*-WSe_2 and *r*-BN.

S2.6. Potential drop and bandgap dependence on stack thickness for 1T' ReS_2, 1T' WTe_2 and $MoTe_2$

The polarization saturation mechanism discussed in the main text is not limited to *r*-MoS_2 layered stacks and can be found in other non-centrosymmetrically stacked 2D materials. For example, in 1T'-ReS_2, the polarization of which was experimentally studied,(*12*) polarization saturation and bandgap closure are predicted to occur at $N = 18$ (see Fig. S10a). While semi-metallic systems, such as 1T' WTe_2 and $MoTe_2$ (Fig. S11b), may exhibit interfacial ferroelectricity,(*13, 14*) no significant dependence on stack thickness is predicted, as expected for zero-bandgap materials.

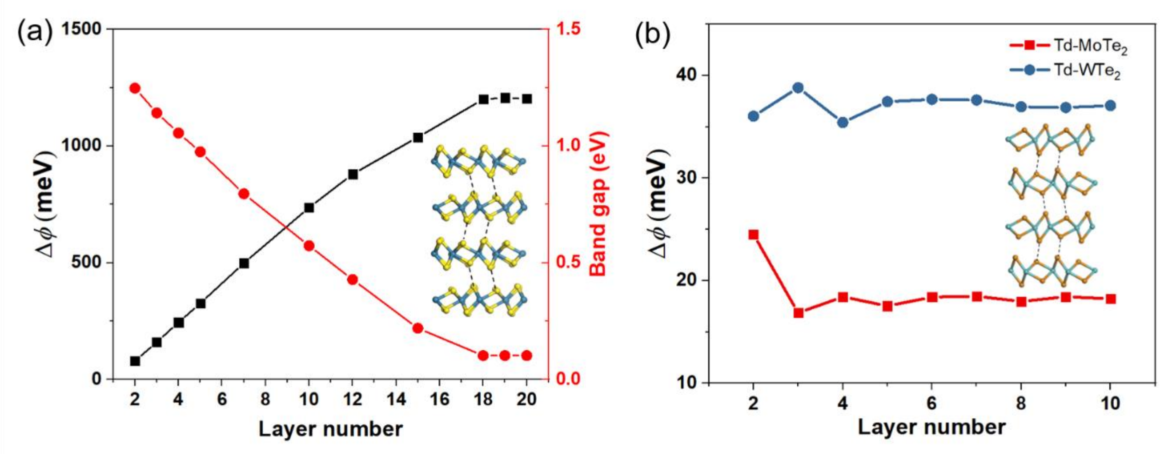

Figure S11. Potential drop and bandgap as a function of the number of layers for 1T' ReS_2, 1T' WTe_2 and $MoTe_2$. (a) DFT-computed potential drop and bandgap calculations of structurally relaxed 1T' ReS_2 as a function of stack thickness. (b) DFT-computed potential drop as a function of layer number in semi-metallic 1T' WTe_2 and $MoTe_2$ multilayers.

S3. Self-consistent solution of the Poisson and Schrödinger equations

We used the following algorithm to obtain self-consistent solutions of the Poisson and Schrödinger equations:

1. We start by creating a simplified periodic function to model polarization-induced charge transfer, $\rho_{pol}(z)$. The corresponding polarization-induced potential, $\phi_{pol}(z)$, is then calculated by solving the one-dimensional (1D) Poisson equation:

$$\frac{d^2\phi_{pol}(z)}{dz^2} = \frac{\rho_{pol}(z)}{\epsilon_0}, \tag{1}$$

where ϵ_0 is the free space permittivity. The magnitude and distribution width of $\rho_{pol}(z)$ are then optimized to mimic the DFT-calculated polarization induced potential variation across the stack. An example of the simplified density profile and the corresponding potential profile, compared to the DFT counterparts, is presented in Figs. S12a,b.

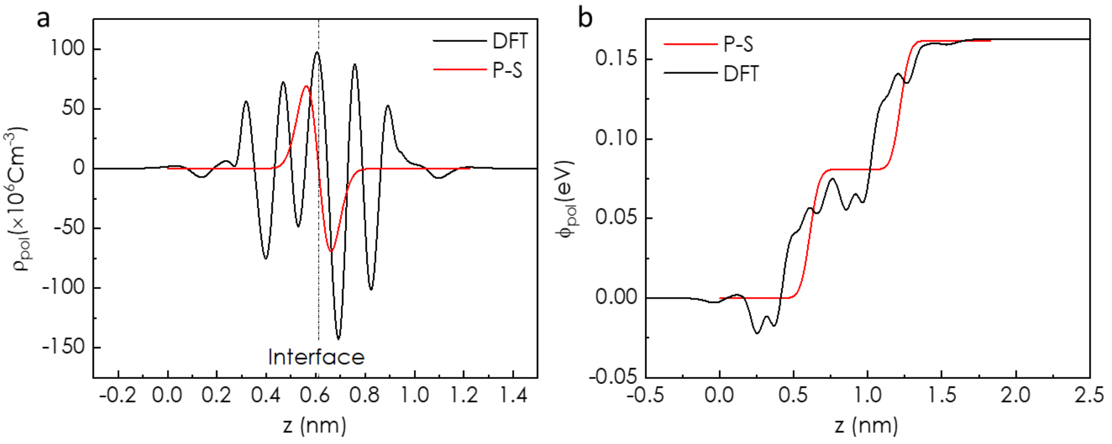

Figure S12. (a) Example of a simplified density profile used in the Poisson-Schrödinger (P-S) calculation (red) compared to the DFT result (black). (b) Corresponding potential profiles obtained from the solution of the Poisson equation.

2. A pair of Schrödinger equations are solved to acquire the spontaneously excited free electron and hole densities:

$$-\frac{\hbar^2}{2m_e^*}\frac{\partial\psi_e^2(z)}{\partial z^2}+V_c(z)\psi_e^n(z)=\mathrm{E}_e^n\psi_e^n(z) \tag{2}$$

$$-\frac{\hbar^2}{2m_h^*}\frac{\partial\psi_h^2(z)}{\partial z^2}+V_v(z)\psi_h^n(z)=\mathrm{E}_h^n\psi_h^n(z) \tag{3}$$

where the conduction and valence band potentials are taken to be $V_c(z)=-e\phi_{pol}(z)$ and $V_v(z)=V_c(z)-E_g$, where E_g is the bandgap of the system, and E_e^n and E_h^n are the nth energy eigenvalues of electrons and holes, respectively. m_e^*, m_h^* are electron and hole effective masses, respectively. We use the effective out-of-plane electron mass at the conduction band Q, $0.49m_e$, and the effective out-of-plane hole mass at the valence band Γ point, $0.80m_e$, (*16*) where m_e is the free electron rest mass. The free electron and hole densities are then calculated via:

$$\rho_e(z)=-e\,g_v\frac{m_e^*k_BT}{\pi\hbar^2}\sum_n\ln\left(1+e^{\frac{E_f-\mathrm{E}_e^n}{k_BT}}\right)|\psi_e^n(z)|^2, \tag{4}$$

$$\rho_h(z)=e\,g_v\frac{m_h^*k_BT}{\pi\hbar^2}\sum_n\ln\left(1+e^{\frac{\mathrm{E}_h^n-E_f}{k_BT}}\right)|\psi_h^n(z)|^2, \tag{5}$$

where k_B is the Boltzmann constant, T (=300K for our calculation) is the temperature, $\hbar$ is the reduced Planck constant, and E_f is the chemical potential. Eqs. (4) and (5) are obtained via integration of the 2D density of states, multiplied by the Fermi-Dirac distribution, along the two unconfined directions.(*15*) The prefactors in the summations, prior to the probability density, accounts for the thermal distribution of free carriers at a finite temperature among available subbands. g_v stands for the valley degeneracy viz. 6 for Q valley of conduction band and 1 for Γ valley of valence band.

3. To obtain a self-consistent solution, $\rho_e(z)$ and $\rho_h(z)$ are added to $\rho_{pol}(z)$ in the Poisson equation as follows:

$$\frac{d^2\phi}{dz^2} = \frac{\rho_{pol}(z)}{\epsilon_0} + \frac{\rho_e(z)+\rho_h(z)+e\,N_d}{\epsilon_0\epsilon_r}, \tag{6}$$

where N_d is the density of positively charged donors and $\epsilon_r = 8.9$ is the relative permittivity of bulk MoS_2.(*17*)

The process is repeated until self-consistency is achieved. If charge neutrality is satisfied the calculation is terminated, otherwise the value of E_f is modified accordingly and the process restarts. SciPy and NumPy Python-libraries were used to perform these numerical calculations. E_g was used as a free parameter to match the V_{kp} saturation value obtained from DFT. A value of 0.64 eV was used for all the results shown in the paper. It remains a constant for all thickness and doping.

We can further define the bandgap as the energy separation between the frontier eigenvalues in the conduction and valence band (see Fig. S13a). Essentially, it is the correction to the classical bandgap, E_g, due to quantum confinement. Interestingly, the bandgap variation as a function of layer number, both for undoped and doped cases, follows a similar trend as that obtained from the DFT calculations.

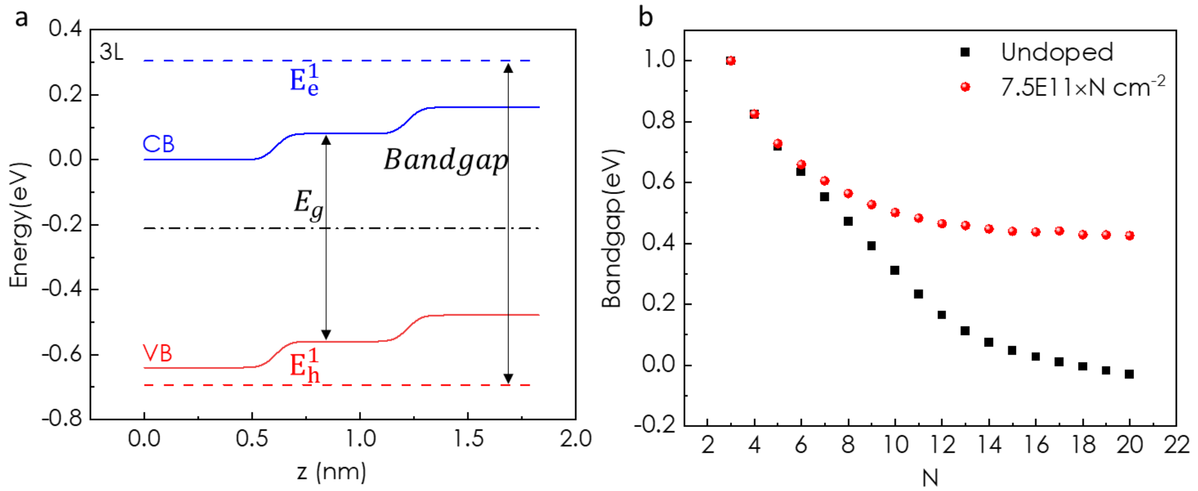

Figure S13. (a) Calculated conduction and valence band profile along an ABC stacked trilayer with co-oriented interfacial polarization. Schematic representation of various parameters used in the self-consistent Poisson-Schrödinger calculation. (b) Variation of bandgap obtained from the frontier orbitals of the self-consistent calculation, as a function of the number of layers for the undoped and electron-doped cases.

References

1. J. Colchero, A. Gil, A. M. Baró, Resolution enhancement and improved data interpretation in electrostatic force microscopy. *Phys. Rev. B* **64**, 245403 (2001).
2. J. P. Perdew, K. Burke, M. Ernzerhof, Generalized gradient approximation made simple. *Phys. Rev. Lett.* **77**, 3865-3868 (1996).
3. S. Grimme, J. Antony, S. Ehrlich, H. Krieg, A consistent and accurate ab initio parametrization of density functional dispersion correction (DFT-D) for the 94 elements H-Pu. *J. Chem. Phys.* **132**, 154104 (2010).
4. G. Kresse, J. Furthmuller, Efficient iterative schemes for ab initio total-energy calculations using a plane-wave basis set. *Phys. Rev. B* **54**, 11169-11186 (1996).
5. G. Makov, M. C. Payne, Periodic boundary conditions in ab initio calculations. *Phys. Rev. B* **51**, 4014-4022 (1995).
6. J. Heyd, G. E. Scuseria, M. Ernzerhof, Hybrid functionals based on a screened Coulomb potential. *J. Chem. Phys.* **118**, 8207-8215 (2003).
7. J. Heyd, G. E. Scuseria, Efficient hybrid density functional calculations in solids: Assessment of the Heyd–Scuseria–Ernzerhof screened Coulomb hybrid functional. *J. Chem. Phys.* **121**, 1187-1192 (2004).
8. J. Heyd, G. E. Scuseria, Assessment and validation of a screened Coulomb hybrid density functional. *J. Chem. Phys.* **120**, 7274-7280 (2004).
9. J. Heyd, G. E. Scuseria, M. Ernzerhof, Erratum: "Hybrid functionals based on a screened Coulomb potential" [J. Chem. Phys. 118, 8207 (2003)]. *J. Chem. Phys.* **124**, 219906 (2006).
10. O. Sinai, L. Kronik, Simulated doping of Si from first principles using pseudoatoms. *Phys. Rev. B* **87**, 235305 (2013).
11. P. Giannozzi *et al.*, QUANTUM ESPRESSO: a modular and open-source software project for quantum simulations of materials. *J. Phys.: Condens. Matter* **21**, 395502 (2009).
12. Y. Wan *et al.*, Room-temperature ferroelectricity in 1T '-ReS_2 multilayers. *Phys. Rev. Lett.* **128**, 067601 (2022).
13. Z. Fei *et al.*, Ferroelectric switching of a two-dimensional metal. *Nature* **560**, 336-339 (2018).
14. A. Jindal *et al.*, Coupled ferroelectricity and superconductivity in bilayer Td-$MoTe_2$. *Nature* **613**, 48-52 (2023).
15. C. Hamaguchi, C. Hamaguchi, *Basic semiconductor physics*. (Springer, 2010), vol. 9.
16. H. Peelaers, C. G. Van de Walle, Effects of strain on band structure and effective masses in MoS_2. *Phys. Rev. B* **86**, 241401 (2012).
17. A. Kumar, P. K. Ahluwalia, Tunable dielectric response of transition metals dichalcogenides MX_2 (M=Mo, W; X=S, Se, Te): Effect of quantum confinement. *Phys. B: Condens. Matter* **407**, 4627-4634 (2012).